Two-dimensional angular distribution of photoelectrons of single-crystal graphite

1996 J. Phys.: Condens. Matter 8 2715

(http://iopscience.iop.org/0953-8984/8/15/020)

J. Phys.: Condens. Matter **8** (1996) 2715–2732. Printed in the UK

Two-dimensional angular distribution of photoelectrons of single-crystal graphite

H Nishimoto, T Nakatani, T Matsushita, S Imada, H Daimon and S Suga

Department of Material Physics, Faculty of Engineering Science, Osaka University, Toyonaka, Osaka 560, Japan

Received 17 July 1995, in final form 31 October 1995

Abstract. Two-dimensional band structures of single-crystalline graphite have been directly observed by using a new version of a two-dimensional display-type spherical mirror analyser. The intensity distribution patterns at various binding energies below the Fermi level for the excitation by linearly polarized synchrotron radiation ($h\nu = 54$ eV) normally incident on the cleaved surface have shown crystal-symmetry-broken angular distributions. The non-sixfold symmetry can be understood as being the result of the angular dependence of the probability of the electric dipole transition from each atomic orbital with a particular symmetry (p_z, p_y, p_x or s) for the s-polarized synchrotron radiation. In order to understand the uneven intensity in different Brillouin zones, we consider a model including the tight-binding initial state and a free-electron-like final state. It is found that such unusual distribution patterns are explained by the new concept of a 'photoemission structure factor' with consideration of the phase of the coefficients of the atomic orbitals of inequivalent atoms in a unit cell in the initial-state Bloch function.

1. Introduction

Measurement of the two-dimensional angular distribution of electrons is an important technique in solid-state physics. For example, the two-dimensional angular distribution of photoelectrons emitted from a crystal surface excited by an ultraviolet light enables us to obtain information on the electronic energy band structure of solids or surfaces [1, 2]. The equivalent measurement in the higher-energy region enables us to obtain information on the surface atomic arrangement by means of photoelectron diffraction (PED) or photoelectron holography experiments [3].

We have developed a new two-dimensional display-type spherical mirror analyser [4], for analysing the kinetic energy as well as the angular distribution of charged particles. Unlike Eastman's display-type analyser [5], which consists of an ellipsoidal electrostatic mirror in addition to six spherical grids, our analyser is exclusively composed of a spherical mirror and grids. This analyser, which operates on a different principle [4], has such advantages as (1) the two-dimensional pattern is measured without distortion and (2) the acceptance cone is as wide as is possible (2π steradians in principle).

For two-dimensional systems, such as surfaces or layered compounds with negligible dispersion along the *c*-axis, this analyser can directly display the constant-energy cross section of the band structure. We chose graphite, whose electronic states have been extensively studied. For example, the energy band structure of graphite has been investigated experimentally using angle-resolved ultraviolet photoemission (ARUPS) [6],

0953-8984/96/152715+18$19.50

inverse photoelectron spectroscopy (IPES) [7], and electron energy-loss spectroscopy (EELS) [8]. Santoni *et al* [9] have measured the Fermi surface and band cross sections by using the Eastman display-type photoelectron spectrometer for a p-polarized synchrotron radiation which was incident at 60° to the surface normal. We employed s-polarized synchrotron radiation normally incident on the surface with the electric field vector within a mirror plane. The symmetry of the photoelectron distribution was carefully measured and an unusual angular distribution of photoelectrons was observed. The observed unusual symmetry in the pattern and, in particular, the inequivalence among different Brillouin zones (BZ) is discussed on the basis of a simulation made by means of a tight-binding approximation.

2. Experimental details

The experiment was performed on the beamline BL-7A of the Photon Factory (PF, a 2.5 GeV positron storage ring) of the National Laboratory for High Energy Physics. This beamline belongs to the Spectra Chemistry Research Centre of the University of Tokyo. The range of photon energy ($h\nu$) covered with a plane grating monochromator is 10–1000 eV. For the energy $h\nu = 54$ eV employed in the experiment, the energy resolution was $h\nu/\Delta h\nu \sim 400$ providing $\Delta h\nu = \pm 0.1$ eV, and the photon flux was about 10^{11} photons s^{-1}. Photons were focused to a spot with a diameter of about 1 mm.

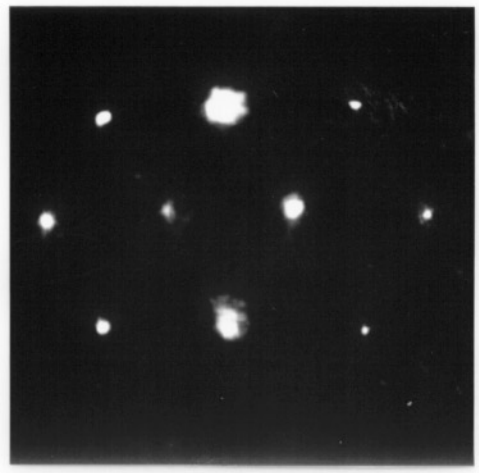

Figure 1. The LEED pattern of kish graphite observed by the two-dimensional display-type spherical mirror analyser. These clear spots indicate that the sample is a good single crystal and does not include differently oriented layers, in contrast to HOPG.

A synthesized single-crystalline graphite (kish graphite) was used for the experiment. The typical crystal size was about $4 \times 6 \times 0.2$ mm^3. The sample was cleaved parallel to the basal plane (perpendicularly to the crystallographic c-axis) in a preparation chamber (1×10^{-9} Torr), and inserted immediately into the analyser chamber. The quality of the sample surface was checked by low-energy electron diffraction (LEED). The sample showed a sharp LEED pattern, as in figure 1. If highly oriented pyrolytic graphite (HOPG) were mixed in to some extent, extra streaks would have appeared passing through the regular spots. Since such streaks were not observed, it was confirmed that the sample was a good single crystal with almost no rotational disorder of layers, in contrast to HOPG.

s-polarized photons were used in our experiment to compare the result with that of Santoni *et al* [9] obtained with the p-polarized light excitation. All of the measurements

were performed in the normal-incidence configuration. The degree of the linear polarization was higher than 90%.

The new version of the two-dimensional display-type spherical mirror analyser [4] was used for the measurements of the two-dimensional angular distribution of photoelectrons as well as of their kinetic energy. This analyser has an angular acceptance of $\pm 50^\circ$ and optimum energy resolution of 0.2 eV (full width at half-maximum, FWHM) for the pass energy of about 10 eV. In this experiment at $h\nu = 54$ eV, the energy resolution of the analyser was set to about 0.5 eV (FWHM). The two-dimensional patterns were measured at several kinetic energies. It took about thirty minutes to measure each angular distribution pattern. The experiments were performed at room temperature under a vacuum of 1×10^{-10} Torr.

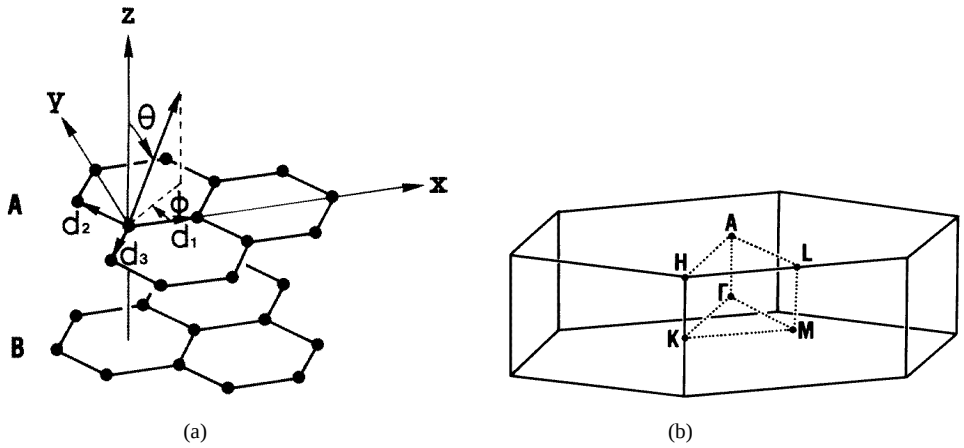

(a) (b)

Figure 2. (a) The crystalline structure of kish graphite and the Cartesian coordinates. The x- and y-axes lie in the hexagonal lattice plane of graphite. The z-axis is normal to the plane. The positions of the nearest-neighbour carbon atoms are given by $\boldsymbol{d}_1$, $\boldsymbol{d}_2$ and $\boldsymbol{d}_3$. (b) The Brillouin zone of graphite. Several high-symmetry points are indicated.

3. Results and discussion

In this paper we adopt the Cartesian coordinate system shown in figure 2(a) for real space for kish graphite. The graphite has an ABAB$\cdots$ stacking sequence. This structure is called 'Bernal structure' [10]. Its hexagonal Brillouin zone (HBZ) is shown in figure 2(b), where one of the Γ–M lines is parallel to the k_x-axis. Each symmetry point is labelled according to the Bouckaert–Smoluchowski–Wigner notation [12]. The polarization of the incident light was parallel to the x-axis ($\boldsymbol{E} \parallel \boldsymbol{x}$).

Figure 3 shows the angle-integrated ultraviolet photoemission (AIUPS) spectrum of the graphite valence band for $h\nu = 54$ eV. Four peaks, i.e., A, B, C and D, are observed in the binding energy (E_B) range between 0 and 20 eV. The two-dimensional patterns were measured at the values of E_B indicated in this figure, from -0.4 to 8.7 eV in nearly 1 eV steps (a–j) and from 11.7 to 19.7 eV in 2 eV steps (k–o).

Hereafter we define the wave vector of the final (initial) state by $\boldsymbol{k}(\boldsymbol{q})$. Figures 4(a)–4(o) show the two-dimensional $(k_x, k_y)_{E_K}$ patterns measured at the energy positions a–o of figure 3, where E_K stands for the photoelectron kinetic energy and (k_x, k_y) are the wave vectors of the electron parallel to the surface which are conserved in the photoemission

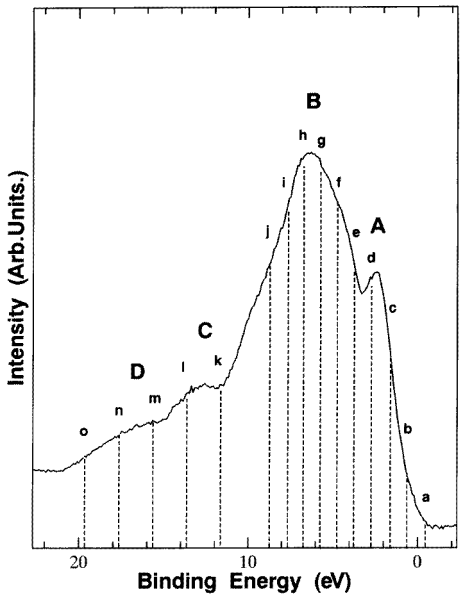

Figure 3. The angle-integrated photoelectron spectrum for single-crystal graphite taken at a photon energy of 54 eV. A, B, C and D represent prominent spectral features. The dashed lines labelled a–o indicate the energy position where the central pass energy of the analyser is set and the two-dimensional angular distribution pattern is measured.

process. k_x corresponds to the horizontal direction in figure 4. Since the coordinates of the originally observed patterns on the 'flat' screen are proportional to ($k_x/\cos\theta$, $k_y/\cos\theta$), the coordinates of figure 4 are given by multiplying by $\cos\theta$. These patterns correspond to the $(q_x, q_y)_{E_B}$ isoenergy contour map of the energy band of graphite. The patterns at different kinetic energies are shown for the common BZ given by the white lines in figure 4. For the measurement of figure 4(a), the pass energy was set at the value which corresponds to the initial-state energy of $E_B = -0.4$ eV (0.4 eV above E_F). Then the shape of the cross section of the band dispersion near the Fermi surface (within about 0.1 eV) can be detected. It took about 40 minutes to measure this pattern. The characteristic feature of this pattern is the appearance of four regions with strong intensity near the vertices of the first BZ. The intensity at the top and bottom vertices is, however, not recognizable. As E_B increases, the four regions near the K points move inward (figure 4(b)) and are prolonged (figure 4(c)). These patterns show that photoelectrons predominantly appear in the first BZ. The adjacent M points on the right- and left-hand sides are bridged as shown in figure 4(d) ($E_B = 2.7$ eV). In figures 4(e), 4(f) and 4(g), corresponding intensities inside the first BZ decrease and the intensities in the right and left second BZ become prominent. Most of the observed $(k_x, k_y)_{E_B}$ behaviour in figures 4(a)–4(f) can be attributed to the 'π-band' dispersion as discussed later.

The prominent intensity near the centre in figures 4(f) and 4(g), and the prominent patterns of 4(h) to 4(l) are associated with bands other than the 'π-band', as explained later. The intensity distribution of these patterns is again not sixfold symmetric and suggests inequivalence of the different BZ. The cross section of the bands shown in the first BZ in figures 4(f)–4(h) has a rectangular shape, and that in figures 4(i) and 4(j) has two strong regions near the vertical axis. In figures 4(k) and 4(l), the signals in the first BZ are weakened and one recognizes stronger signals in the second BZ and near the K symmetry points.

Figures 4(m)–4(o) show the cross section of another band as discussed below. Only these three patterns (m, n and o) are subjected to a pattern-averaging process assuming

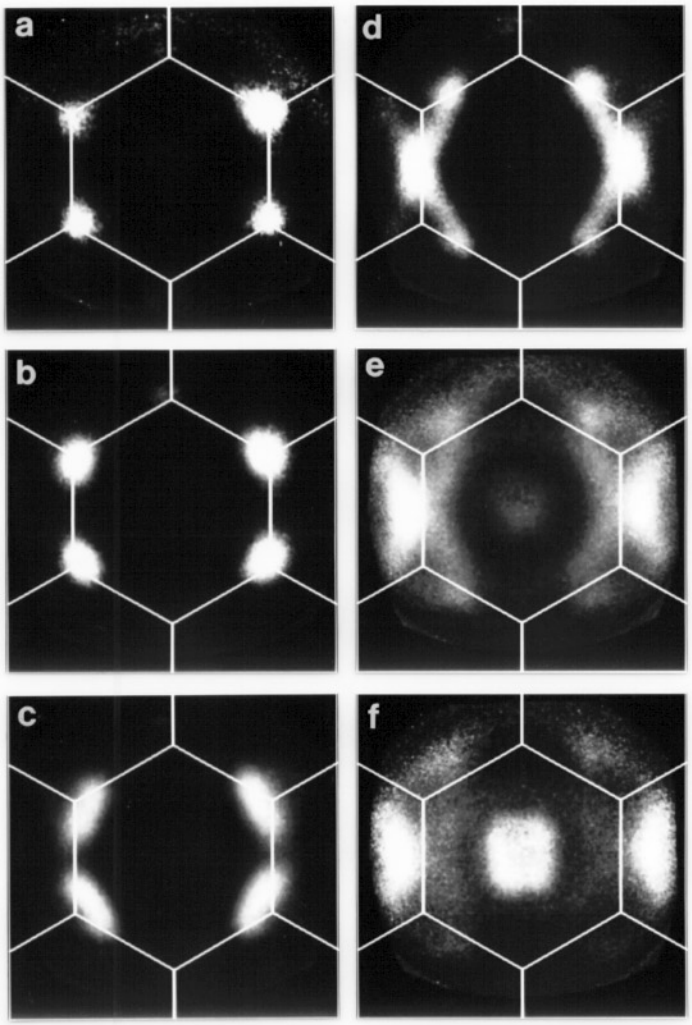

Figure 4. Photoelectron angular distribution patterns of kish graphite measured by the two-dimensional display-type spherical mirror analyser. White lines show the boundaries of the Brillouin zones. (a)–(o) show the cross sectional patterns at the energies labelled a–o in figure 3 ((a): −0.4; (b): 0.7; (c): 1.7; (d): 2.7; (e): 3.7; (f): 4.7; (g): 5.7; (h): 6.7; (i): 7.7; (j): 8.7; (k): 11.7; (l): 13.7; (m): 15.7; (n): 17.7; and (o): 19.7 eV). See the text for details.

mirror symmetry with respect to the central vertical and horizontal lines (other patterns, (a)–(l), give the originally recorded intensity distribution corrected for $\cos\theta$). This treatment is employed because the exit aperture position of the analyser was optimized to the highest-E_K photoelectrons, and the patterns, (m)–(o), of low-E_K electrons have shown some deviation from the twofold symmetry as demonstrated in figure 4(l). From figure 4(m) to figure 4(o), the pattern shrinks inward, although the intensity remains near the M points on the left- and right-hand sides.

It is known that the electronic bands of kish graphite are characterized by the symmetry of the contributing atomic orbitals. The bands are often called π-, σ_3-, σ_2- and σ_1-bands with increasing E_B near the M point. The broken lines in figure 5 show the bands calculated

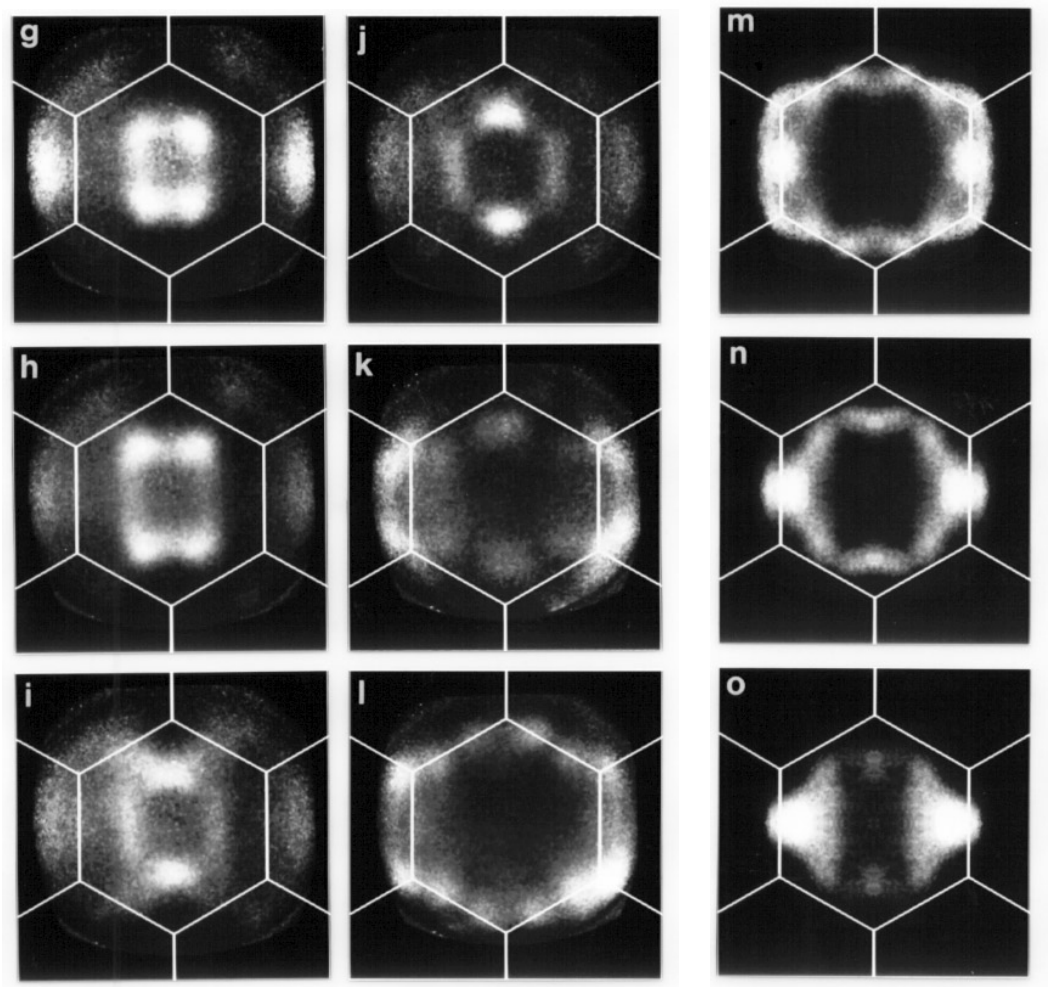

Figure 4. (Continued)

by Tatar and Rabii using the KKR method [13]. The π-band is made from the $2p_z$ orbital of the carbon atom and split into two bands because there are two layers, A, B, in a unit cell. Although the $\sigma_3(2p_y)$-, $\sigma_2(2p_x)$- and $\sigma_1(2s)$-bands are made from two bands like the π-band, they are almost degenerate because of a smaller interaction with neighbouring layers due to the in-plane character of their orbitals. The Fermi surface of kish graphite is suggested to lie at the K point in figure 5. The open symbols and crosses show the experimental results from published reports (double circles for [14], circles for [7], triangles for [6] and crosses for [15]). The full circles show the present results; details are given later.

The present result for the 'π-band' is very different from that given by Santoni *et al* [9] with respect to the symmetry of the photoelectron distribution. Although they observed photoelectron distributions with almost sixfold symmetry (after their distortion correction) reflecting the crystal symmetry, our result has only twofold symmetry. It should be remembered that we employed the s-polarized light along the x-axis in the normal-incidence configuration, whereas they employed the p-polarized light.

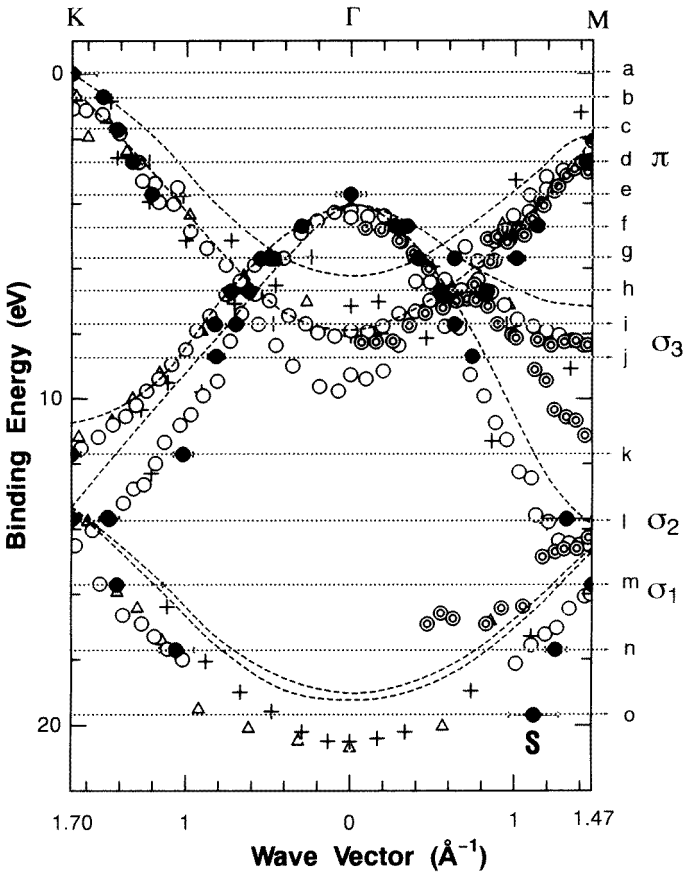

Figure 5. The band structure of kish graphite. The broken lines show the bands calculated by Tatar and Rabii using the KKR method [13]. The π-, σ_3-, σ_2- and σ_1-bands are mainly derived from the $2p_z$, $2p_y$, $2p_x$ and 2s orbitals of the carbon atom, respectively. It is suggested that the Fermi surface of kish graphite lies at the K point. The full circles show the present results. Other marks show experimental results from published reports (double circles for [14], circles for [7], triangles for [6] and crosses for [15]).

4. A contour plot of the energy band

Here we consider the energy dispersion of the π-band within the tight-binding approximation to provide a basis on which to discuss the photoemission intensity distribution. The energy eigenvalue E of the π-band for one monolayer of graphite is obtained from the secular equation in the tight-binding approximation as follows:

$$\det|\mathbf{T} - E\mathbf{S}| = 0 \tag{1}$$

where the transfer matrix $\mathbf{T}$ and the overlap matrix $\mathbf{S}$ are represented as

$$\mathbf{T} = \begin{bmatrix} \epsilon_p & (\epsilon_p s_{pp\pi} + t_{pp\pi})g \\ (\epsilon_p s_{pp\pi} + t_{pp\pi})g^* & \epsilon_p \end{bmatrix} \qquad \mathbf{S} = \begin{bmatrix} 1 & s_{pp\pi}g \\ s_{pp\pi}g^* & 1 \end{bmatrix}. \tag{2}$$

In these formulae, $t_{pp\pi}$ and $s_{pp\pi}$ are the transfer integral and the overlap integral between the p_z orbitals of the nearest-neighbour atoms. ϵ_p is the energy eigenvalue of the atomic

$2p_z$ state. The coefficient g is defined by

$$g(\boldsymbol{q}) = e^{i\boldsymbol{q}\cdot\boldsymbol{d}_1} + e^{i\boldsymbol{q}\cdot\boldsymbol{d}_2} + e^{i\boldsymbol{q}\cdot\boldsymbol{d}_3} \tag{3}$$

where $\boldsymbol{q} = (q_x, q_y, q_z)$ is the electron wave vector, and $\boldsymbol{d}_1, \boldsymbol{d}_2$ and $\boldsymbol{d}_3$ are the position vectors of the nearest-neighbour carbon atoms (figure 2(a)) as given by $\boldsymbol{d}_1 = (d, 0, 0)$, $\boldsymbol{d}_2 = (-d/2, d\sqrt{3}/2, 0)$, $\boldsymbol{d}_3 = (-d/2, -d\sqrt{3}/2, 0)$, where d is taken as 1.42 Å. All carbon atoms are classified into two inequivalent types of site (A_1 and A_2). The atom at the origin belongs to an A_1 site and the atom at $\boldsymbol{d}_1$ belongs to an A_2 site.

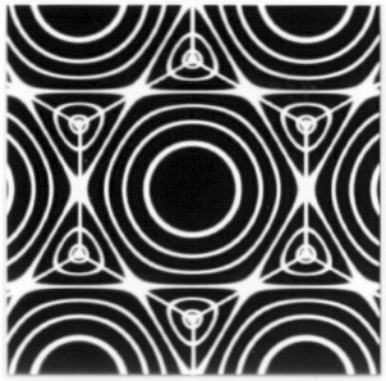

Figure 6. Contour lines of the π-band of kish graphite calculated by assuming $t_{pp\pi} = -3.03$ eV, $s_{pp\pi} = 0.129$ and $\epsilon_p = 0$ eV [11]. The centre corresponds to the Γ point. The corners surrounded by the small circles ($E_B = 0.7$ eV) correspond to the K points. The central binding energies of the lines are 0.7, 1.7, 2.7, 3.7, 4.7 and 5.7 eV, and the energy width is taken to be ± 0.1 eV.

The two-dimensional dispersion of the π-bonding band $E(q_x, q_y)$ is obtained as $[\epsilon_p + (\epsilon_p s_{pp\pi} + t_{pp\pi})|g|]/(1 + s_{pp\pi}|g|)$. The constant-energy cross sections (or contours) for $t_{pp\pi} = -3.03$ eV, $s_{pp\pi} = 0.129$ and $\epsilon_p = 0$ eV [11] calculated for E_B from 0.7 to 5.7 eV in 1 eV steps for comparison with the present experiment are shown in figure 6. We can assume that the photon wave vector $\boldsymbol{Q}$ is negligible and that the momentum parallel to the surface is conserved in the photoemission process, where the photoelectron has the $\boldsymbol{k}$-vector with (k_x, k_y) components given by the initial states (q_x, q_y), whereas k_z is determined by the kinetic energy E_K. E_K is determined by the energy conservation rule given by $E_K = h\nu - E_B - \Phi$ (Φ stands for the work function). The photoemission intensities at different $\boldsymbol{k}$ are, however, not uniform but are determined by the transition probabilities as discussed in the next section. Although considerable parts of the contours in figure 6 are not seen in the experimental results, the calculated shape and its energy dependence are in reasonable accordance with the observed result. For example, the photoemission near the Fermi level (E_F) is observed near the K point and then moves inward with increasing E_B and bridges to the adjacent M points. Some discrepancies recognized between figures 4(a)–4(e) and figures 6 are as follows. (1) The position of the centre of gravity of the photoemission signals within 0.1 eV from E_F given in figure 4(a) is not just on the K point but slightly inside the first BZ, whereas figure 6 shows a threefold symmetry around the K point. (2) The calculation has shown that the contour circle of the π-band would shrink towards the Γ point with increasing E_B as predicted in figure 6 for $E_B = 3.7$, 4.7 and 5.7 eV. Such behaviour was not directly observed in the first BZ although it was observed to some extent in the second BZ on the left- and right-hand sides in figures 4(e), 4(f) and 4(g). The spacings between these contours in (e), (f) and (g) are narrower in the observed pattern than those in the theoretical calculation.

5. Intensity distribution analysis

In order to interpret the symmetry-broken properties of the two-dimensional photoelectron distributions, we will calculate the angular dependence of the probability of transition from the tight-binding initial state of the π-band in the so-called one-step model.

The eigenfunction of the π-bonding band is also obtained from equation (1) as

$$\Psi(\boldsymbol{q},\boldsymbol{r}) = \frac{1}{\sqrt{N}}\sum_n \frac{\mathrm{e}^{\mathrm{i}\boldsymbol{q}\cdot\boldsymbol{R}_n}}{\sqrt{\lambda}}\left(\frac{g}{|g|}\phi(\boldsymbol{r}-\boldsymbol{R}_n)+\mathrm{e}^{\mathrm{i}\boldsymbol{q}\cdot\boldsymbol{d}_1}\phi(\boldsymbol{r}-\boldsymbol{R}_n-\boldsymbol{d}_1)\right)$$
$$= \frac{1}{\sqrt{N}}\sum_{n,j}\mathrm{e}^{\mathrm{i}\boldsymbol{q}\cdot(\boldsymbol{R}_n+\boldsymbol{t}_j)}c_j(\boldsymbol{q})\phi(\boldsymbol{r}-\boldsymbol{R}_n-\boldsymbol{t}_j) \tag{4}$$

where $\lambda = 2(1+s_{\mathrm{pp}\pi}|g|)$, $\boldsymbol{R}_n$ is the lattice vector of the nth unit cell, and $\boldsymbol{t}_j$ is the position vector of the jth inequivalent atom in the unit cell. Thus $\phi(\boldsymbol{r}-\boldsymbol{R}_n)$ and $\phi(\boldsymbol{r}-\boldsymbol{R}_n-\boldsymbol{d}_1)$ are the atomic orbitals of two inequivalent atoms in a unit cell expressed using a spherical harmonic $Y_{lm}(\theta,\phi)$ as $\phi(\boldsymbol{r}) = R_{nl}(r)Y_{lm}(\theta,\phi)$. Here $R_{nl}(r)$ is a radial function [16], and l and m stand for the orbital angular momentum and its z-component, taking the z-axis parallel to the c-axis of the crystal. θ and ϕ are given in figure 2(a). In this treatment, the spin is neglected because it is conserved in the dipole excitation. In the case of the π-band, $\phi(\boldsymbol{r})$ is a p_z orbital, and the spherical harmonic is written as $Y_{10}(\theta,\phi) = (3/4\pi)\cos\theta$. This function $\Psi(\boldsymbol{q},\boldsymbol{r})$ corresponds to the initial state $|i\rangle$ of the transition. We represent the final state in the crystal by $|f_{\boldsymbol{k}}(\boldsymbol{r})\rangle$ which is a Bloch function with $\boldsymbol{k}$.

The transition operator, or the perturbation term, H', is represented by

$$H' = -(e/mc)\boldsymbol{p}\cdot\boldsymbol{A}.$$

Here $\boldsymbol{p}$ is the momentum operator, $-\mathrm{i}\hbar\boldsymbol{\nabla}$, and $\boldsymbol{A}$ is the vector potential of the incident light. e and m are the charge and the mass of the electron and c is the light velocity. $\boldsymbol{A}$ is written as $\boldsymbol{A} = A_0\boldsymbol{e}\,\mathrm{e}^{\mathrm{i}\boldsymbol{Q}\cdot\boldsymbol{r}}$, where A_0 is a constant and $\boldsymbol{e}$ is the polarization unit vector of the light. The time dependence of the vector potential is given by the real part of $\boldsymbol{A}\mathrm{e}^{-\mathrm{i}2\pi\nu t}$, where t is the time.

Here, we express the dipole matrix element M as $M = \langle f_{\boldsymbol{k}}(\boldsymbol{r})|H'|i\rangle$. Using the above formula (4) for $|i\rangle$, M is written as

$$M \propto \frac{1}{\sqrt{N}\sqrt{\lambda}}\sum_n \mathrm{e}^{\mathrm{i}\boldsymbol{q}\cdot\boldsymbol{R}_n}\frac{g}{|g|}\langle\mathrm{e}^{-\mathrm{i}\boldsymbol{Q}\cdot\boldsymbol{r}}f_{\boldsymbol{k}}(\boldsymbol{r})|\boldsymbol{p}\cdot\boldsymbol{e}|\phi(\boldsymbol{r}-\boldsymbol{R}_n)\rangle$$
$$+\frac{1}{\sqrt{N}\sqrt{\lambda}}\sum_n \mathrm{e}^{\mathrm{i}\boldsymbol{q}\cdot\boldsymbol{R}_n}\mathrm{e}^{\mathrm{i}\boldsymbol{q}\cdot\boldsymbol{d}_1}\langle\mathrm{e}^{-\mathrm{i}\boldsymbol{Q}\cdot\boldsymbol{r}}f_{\boldsymbol{k}}(\boldsymbol{r})|\boldsymbol{p}\cdot\boldsymbol{e}|\phi(\boldsymbol{r}-\boldsymbol{R}_n-\boldsymbol{d}_1)\rangle. \tag{5}$$

Since $f_{\boldsymbol{k}}(\boldsymbol{r})$ is a Bloch function, the first term in equation (5) is rewritten by changing the variable and using the Kronecker delta symbol as

$$\sum_{\boldsymbol{G}}\frac{\sqrt{N}}{\sqrt{\lambda}}\delta_{\boldsymbol{k}-\boldsymbol{Q}-\boldsymbol{q},\boldsymbol{G}}\frac{g}{|g|}\langle\mathrm{e}^{-\mathrm{i}\boldsymbol{Q}\cdot\boldsymbol{r}}f_{\boldsymbol{k}}(\boldsymbol{r})|\boldsymbol{p}\cdot\boldsymbol{e}|\phi(\boldsymbol{r})\rangle. \tag{6}$$

The second term is also rewritten as

$$\sum_{\boldsymbol{G}}\frac{\sqrt{N}}{\sqrt{\lambda}}\delta_{\boldsymbol{k}-\boldsymbol{Q}-\boldsymbol{q},\boldsymbol{G}}\mathrm{e}^{-\mathrm{i}\boldsymbol{G}\cdot\boldsymbol{d}_1}\langle\mathrm{e}^{-\mathrm{i}\boldsymbol{Q}\cdot\boldsymbol{r}}f_{\boldsymbol{k}}(\boldsymbol{r})|\boldsymbol{p}\cdot\boldsymbol{e}|\phi(\boldsymbol{r})\rangle. \tag{7}$$

Here, $\boldsymbol{G}$ is the reciprocal-lattice vector. As the wave vector $\boldsymbol{Q}$ of the photon used is very small compared with the size of the BZ of kish graphite, we will neglect $\boldsymbol{Q}$ hereafter. Since the Umklapp process is negligible in the present experimental results as recognized from

the negligible intensity near the top and bottom vertices in figure 4, we can take $\boldsymbol{G} = 0$ and $\boldsymbol{q} = \boldsymbol{k}$. Then,

$$M \propto \frac{\sqrt{N}}{\sqrt{\lambda}} \left(\frac{g(\boldsymbol{k})}{|g(\boldsymbol{k})|} + 1 \right) \langle f_{\boldsymbol{k}}(\boldsymbol{r}) | \boldsymbol{p} \cdot \boldsymbol{e} | \phi(\boldsymbol{r}) \rangle \,. \tag{8}$$

Hence, the intensity distribution $I(\theta_{\boldsymbol{k}}, \phi_{\boldsymbol{k}})$, except for the energy conservation term, is expressed as

$$I(\theta_{\boldsymbol{k}}, \phi_{\boldsymbol{k}}) \propto |M_C(\boldsymbol{k})|^2 \, |M_A(\boldsymbol{k})|^2 \tag{9}$$

where

$$M_C(\boldsymbol{k}) = \frac{g(\boldsymbol{k})/|g(\boldsymbol{k})| + 1}{\sqrt{\lambda}} = \sum_j c_j(\boldsymbol{k}) \tag{10}$$

$$M_A(\boldsymbol{k}) = \langle f_{\boldsymbol{k}}(\boldsymbol{r}) | \boldsymbol{p} \cdot \boldsymbol{e} | \phi(\boldsymbol{r}) \rangle \,. \tag{11}$$

Equation (10) is a simple sum of the coefficients of the wave function in equation (4). $c_j(\boldsymbol{k})$ represents the phase and amplitude of the atomic orbitals of the crystallographically inequivalent atomic sites. Hence this term $|M_C(\boldsymbol{k})|^2$ represents an interference induced by the phase difference in the coefficients of the atomic orbitals in the initial-state Bloch function. Note that this interference is not due to the path-length difference between two photoelectron waves from the two inequivalent atoms. This term is very important and provides the new effect as recognized when we compare intensities of the first and second BZ, and will be discussed below in detail. On the other hand, the term $|M_A(\boldsymbol{k})|^2$ represents the photoelectron angular distribution from the atomic orbital.

5.1. The photoelectron angular distribution from atomic orbitals

We first examine the effect of $|M_A(\boldsymbol{k})|^2$ for the major angular dependence. We now replace $\boldsymbol{p} \cdot \boldsymbol{e}$ with $\boldsymbol{e} \cdot \boldsymbol{r}$ in the calculation of $M_A(\boldsymbol{k})$ from the atomic orbital. This is, however, an approximation since the atomic orbital, $\phi(\boldsymbol{r})$, is not an eigenfunction of the system. The operator $\boldsymbol{e} \cdot \boldsymbol{r}$ can be represented in terms of the spherical harmonics as

$$\boldsymbol{e} \cdot \boldsymbol{r} = \sum_{\mu=-1}^{1} \sqrt{(4\pi/3)} \, e_\mu Y_{1\mu}(\theta, \phi) r$$

where $e_{\pm 1} = (\mp e_x + \mathrm{i} e_y)/\sqrt{2}$, $e_0 = e_z$. If we assume that the final state is free-electron like outside the muffin-tin sphere around the atom which emits the photoelectron, $|f_{\boldsymbol{k}}(\boldsymbol{r})\rangle$ can be represented as

$$|f_{\boldsymbol{k}}(\boldsymbol{r})\rangle = 4\pi \sum_{l'm'} (\mathrm{i})^{l'} \mathrm{e}^{-\mathrm{i}\delta_{l'}} Y^*_{l'm'}(\theta_{\boldsymbol{k}}, \phi_{\boldsymbol{k}}) Y_{l'm'}(\theta, \phi) G_{l'}(r)$$

by means of partial-wave expansion [16, 17]. Here $G_{l'}(r)$ stands for a radial wave function which is properly solved within the spherically symmetric muffin-tin potential.

Then the electric dipole excitation probability $|M_A(\boldsymbol{k})|^2$ for excitation from the atomic orbital to the direction of $\boldsymbol{k}$ is represented as

$$|M_A(\boldsymbol{k})|^2 = \left| \sum_{l'=l\pm 1} R(nl \to kl') \sum_{\mu=-1}^{1} e_\mu Y_{l'm+\mu}(\theta_{\boldsymbol{k}}, \phi_{\boldsymbol{k}}) c^1(l'm + \mu, lm) \right|^2$$

with the use of the partial-wave expansion. This is a general formula for the photoelectron transition probability for transitions to the direction $\boldsymbol{k}$ from the atomic orbital having an angular part $Y_{lm}(\theta, \phi)$. Here $R(nl \to kl')$ is the integral of the radial part, which is a

constant number depending on l and l'. $c^1(l'm', lm)$ is the Gaunt coefficient [16]† which is proportional to the Clebsch–Gordan coefficient.

Since the electric vector is along the x-axis in the present experiment, only e_x is non-zero and is represented as $-e_{+1}/\sqrt{2} + e_{-1}/\sqrt{2}$. So μ can be either $+1$ or -1. When the initial state is the p_z atomic orbital for the π-band, its quantum number is $(l, m) = (1, 0)$. Therefore, we have

$$|M^{\pi}_{p_z}(\boldsymbol{k})|^2 \propto \left| \sum_{l'=l\pm1} R(nl \to kl')\{-Y_{l'1}(\theta_{\boldsymbol{k}}, \phi_{\boldsymbol{k}})c^1(l'1, 10) + Y_{l'-1}(\theta_{\boldsymbol{k}}, \phi_{\boldsymbol{k}})c^1(l' -1, 10)\} \right|^2 .$$

In accord with the dipole selection rule, l' can be either 2 or 0. In the present case, however, only the $l' = 2$ state is realized because the final state has either m' $(= m + \mu) = +1$ or $m' = -1$. Since the two Gaunt coefficients have the same value, $c^1(2, -1, 1, 0) = c^1(2, 1, 1, 0) = -\sqrt{3/15}$, we obtain the following relation:

$$|M^{\pi}_{p_z}(\boldsymbol{k})|^2 \propto |-Y_{21}(\theta_{\boldsymbol{k}}, \phi_{\boldsymbol{k}}) + Y_{2-1}(\theta_{\boldsymbol{k}}, \phi_{\boldsymbol{k}})|^2 \propto |\sin\theta_{\boldsymbol{k}} \cos\theta_{\boldsymbol{k}} \cos\phi_{\boldsymbol{k}}|^2$$

as reported in [18].

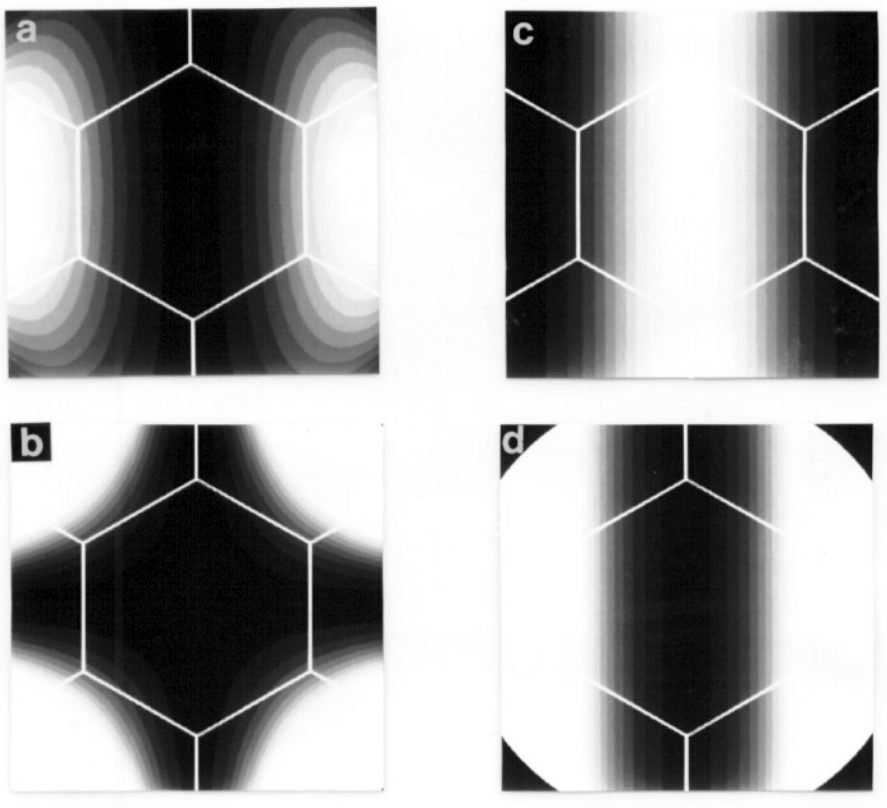

Figure 7. (a), (b), (c) and (d) show the electric dipole excitation probabilities $|M^{\pi}_{p_z}(\boldsymbol{k})|^2$, $|M^{\sigma_3}_{p_y}(\boldsymbol{k})|^2$, $|M^{\sigma_2}_{p_x}(\boldsymbol{k})|^2$ and $|M^{\sigma_1}_{s}(\boldsymbol{k})|^2$ for excitation from the p_z, p_y, p_x and s atomic orbitals, which are the bases of the π-, σ_3-, σ_2- and σ_1-bands, respectively.

† $c^k(l'm', lm) = \sqrt{4\pi/(2k+1)} \int\int Y^*_{l'm'}(\theta, \phi) Y_{k\,m'-m}(\theta, \phi) Y_{l\,m}(\theta, \phi) \sin\theta \; \mathrm{d}\theta \; \mathrm{d}\phi$.

This angular dependence has been calculated and is shown in figure 7(a) for $E_K = 50$ eV. Figure 7(a) demonstrates that the photoelectrons are not emitted within the y–z plane (with $\phi_k = \pm\pi/2$), which corresponds to the central vertical zone in figures 4(a)–4(f). The bright regions in figure 7(a) are in good correspondence with those areas observed in figures 4(a)–4(d). It is clear from this argument that the peaks near the centre (or vertical central zone) of the first BZ in figures 4(f)–4(k) are not from the π-band but may be from the σ_3- and σ_2-bands. The sixfold crystal symmetry is not observed for the photoemission from either of these bands.

The wave functions of the σ_3-, σ_2- and σ_1-bands at the Γ point are almost pure p_y, p_x and s atomic orbitals, respectively. Therefore, their photoemission angular distributions are derived from these atomic orbitals as

$$\left|M^{\sigma_3}_{p_y}(\boldsymbol{k})\right|^2 \propto \left|-Y_{22}\sqrt{\frac{6}{15}} + Y_{2-2}\sqrt{\frac{6}{15}}\right|^2 \propto \left|\sin^2\theta_k \sin 2\phi_k\right|^2 \tag{12}$$

$$|M^{\sigma_2}_{p_x}(\boldsymbol{k})|^2 \propto \left|e^{i\delta_2}R_2\left\{\sqrt{\frac{6}{15}}(Y_{22}+Y_{2-2}) - \frac{2}{\sqrt{15}}(Y_{20})\right\} + e^{i\delta_0}\frac{2R_0}{\sqrt{3}}Y_{00}\right|^2 \tag{13}$$

and

$$|M^{\sigma_1}_{s}(\boldsymbol{k})|^2 \propto \left|-Y_{11}\sqrt{\frac{1}{3}} + Y_{1-1}\sqrt{\frac{1}{3}}\right|^2 \propto |\sin\theta_k \cos\phi_k|^2 \tag{14}$$

where δ_2 and δ_0 are phase shifts and R_2 and R_0 are the radial dipole matrix elements connecting the $l = 1$ and $l' = 2$ states and connecting the $l = 1$ and $l' = 0$ states, respectively. Angular distributions of the photoemission from the $p_y(\sigma_3)$, $p_x(\sigma_2)$ and $s(\sigma_1)$ orbitals calculated for $E_K = 50$ eV are shown in figures 7(b), 7(c) and 7(d), respectively. For the calculation of $|M^{\sigma_2}_{p_x}(\boldsymbol{k})|^2$ in figure 7(c), we tentatively employed the values of $\delta_0 = 6.160$, $\delta_2 = 2.996$, $R_0 = 0.185$ and $R_2 = 0.645$ given for $h\nu = 40.8$ eV for the C 2p state [16]. For $|A^{\sigma_3}_{p_y}(\boldsymbol{k})|^2$ in figure 7(b), the azimuthal angle dependence is represented by $\sin^2 2\phi_k$, which vanishes for $\phi_k = 0, \pm\pi/2$ and π. Among the six directions of the Γ–M axes with $\phi_k = (\pi/3)n$ (n is an integer), only four directions with $\phi_k = \pm\pi/3, \pm 2\pi/3$ may be observable according to equation (12). Besides this, $|M^{\sigma_2}_{p_x}(\boldsymbol{k})|^2$ in figure 7(c) is strong near the central vertical line, in contrast to $|M^{\sigma_3}_{p_y}(\boldsymbol{k})|^2$ in figure 7(b).

Using these extinction rules for the photoelectron excitation from the atomic orbitals, we explain the observed patterns in the first BZ and try to separate the contributions from various atomic orbitals, other than the π-band, in the observed patterns of figure 4. The rectangular shape in figures 4(g) and 4(h) is interpreted as being a result of the superposition of the signals from the σ_2- and σ_3-bands from its energy dependence. Since the intensity is the strongest on the Γ–M axes for $\phi_k = \pm\frac{1}{3}\pi$ and $\pm\frac{2}{3}\pi$ in figures 4(g) and 4(h), we plot the centre of gravity of these regions in figure 5. The plotted results are in good agreement with other experimental results for the σ_3-state. If we plot the centre of gravity of the photoemission signal region on the horizontal Γ–M axis as well as on the vertical Γ–K axis in figures 4(g)–4(j) in figure 5, the positions are near the dispersions of the σ_2-band. On going from figure 4(i) to figure 4(j), the signals near the corners of the rectangle or the Γ–M axes for $\phi_k = \pm\frac{1}{3}\pi$ and $\pm\frac{2}{3}\pi$ disappear. This can be explained consistently, because the band minimum of the σ_3-band on the Γ–M axes is energetically higher than the energy corresponding to (j), which is also confirmed in figure 5.

Before going on with a similar discussion, we check the present argument on the $|M_A(\boldsymbol{k})|^2$ pattern shown in figures 7(a)–7(d). In the first place, we interpret the strong

signals on the Γ–K axis with $\phi_k = \pm\pi/2$ in figure 4(j) as surely arising from the σ_2-band according to the patterns shown in figures 7(b) and 7(c). Next we explain the rectangular pattern in figures 4(g) and 4(h) as being composed of contributions of both the σ_3- and σ_2-bands. As explained before, the σ_3-state provides strong signals on the Γ–M axes. Among these, the signals on the horizontal Γ–M axis are strongly suppressed according to figure 7(b). On the other hand, the σ_2-state provides the signals on the vertical and horizontal axes as demonstrated in figures 4(i) and 4(j). The intensity on both the right- and left-hand sides is, however, weaker than in the central zone according to figure 7(c). We have already interpreted such rectangular shapes in figures 4(g) and 4(h) as due to the superposition of the strong σ_3-signal for $\phi_k = \pm\frac{1}{3}\pi$ and $\pm\frac{2}{3}\pi$ and the weaker σ_2-signal on the right- and left-hand sides. In fact, the photoemission intensity from the $p_x^{\sigma_2}$ orbital for the x-polarization excitation is not so strong even for the $\phi_k = \pm\pi/2$ direction or in the y–z plane, though the white–black representation in figure 7(c) suggests the preferential intensity distribution in the central vertical zone. Therefore, the σ_2-signal on the vertical Γ–K axis is obscured in figures 4(g) and 4(h) by the contributions of the strong σ_3-signals on the nearby Γ–M axes.

In figures 4(i)–4(k), the contours of both the σ_3- and σ_2-bands appear on the Γ–K axes as suggested by the calculated band dispersion. In figure 4(k), one observes two regions of photoemission on the Γ–K axes with $\phi_k = \pm\pi/6$ and $\pm 5/6\pi$. The stronger signals are closer to the K points on the left- and right-hand sides. Corresponding signals are not observed for $\phi_k = \pm\pi/2$. So these signals are definitely assigned to the σ_3-band. On the other hand, much weaker signals are observed for the Γ–K directions in the first BZ. Judging from the dispersion in figure 5 and the intensity distribution in figure 7(c), these weaker signals are assigned to the σ_2-band. In figure 4(l), signals are observed very near the BZ edges. One observes two signal regions on each zone boundary connecting two adjacent K points. One cannot expect a contribution from the σ_3-state in this region of E_B. Consequently, the observed result suggests that the σ_2-band has critical points near the BZ boundary in this energy region and that their bottom energies are deeper than those at the K critical points.

In figures 4(m), 4(n) and 4(o), strong photoemission signals are observed at the M points on the left- and right-hand sides. The energy of the centre of gravity of the signals is plotted in figure 5. With the increase of E_B in going from 4(m) to 4(o), the bright region moves inward as expected for the σ_1-band state (figure 5). The absence of noticeable photoemission intensity near $\phi_k = \pm\pi/2$ in figure 4(o) is in agreement with the predicted angular distribution $|A_s^{\sigma_1}(\boldsymbol{k})|^2$ given in figure 7(d) for the s state. The upper and lower signals at $\phi_k = \pm\pi/2$ in figures 4(m) and 4(n) cannot be simply explained by equation (14). One notices, however, that equation (14) is for the atomic s orbital but not for the entire σ_1-state. This formula is correct near the Γ points where the band is composed of only the s orbital, but it collapses at off-Γ points when any other state is hybridized. In the three σ-bands, p_x, p_y and s orbitals can hybridize with each other, while the entire π-band is composed of only the p_z orbital. As suggested by the band dispersions in figure 5, the p_x and s states are strongly hybridized in σ_2- and σ_1-bands near the BZ boundary. Hence, the $\boldsymbol{k}$-selection rule given by equation (13) for the p_x state can be partly applicable to the angular distribution of the $\sigma_1(\boldsymbol{k})$-state near the M and K points. Thus one observes signals of the σ_1-band even in the central vertical zone. In both figures 4(m) and 4(n), photoemission signals are also observed in the zone connecting the adjacent M points. Then one can plot the central energy of the zone to evaluate the band dispersion along the Γ–K axis. The results for figures 4(m) and 4(n) are in reasonable agreement with other experimental results. If one plots the centre of gravity of the photoemission signals of figure 4(o) in figure 5 as indicated by '$\boldsymbol{S}$', it is

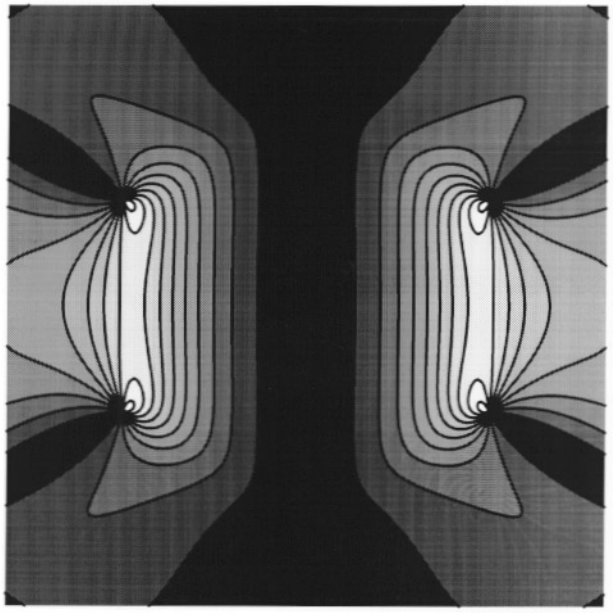

(a)

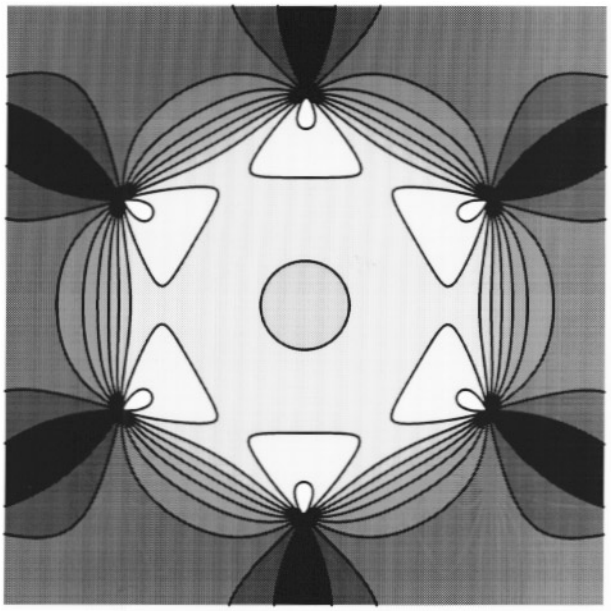

(b)

Figure 8. (a) The photoelectron angular distribution $I^{\pi}(\theta_{\boldsymbol{k}}, \phi_{\boldsymbol{k}})$ of the π-band at $E_{\mathrm{K}} = 50$ eV calculated using equation (15). (b) The 'structure factor of photoemission' $|M_C(\boldsymbol{k})|^2$ in the first and second Brillouin zones, where $M_C(\boldsymbol{k})$ represents the interference between the two photoelectron waves as given by equation (10). The intensity is divided into 11 regions on linear scales. The boundary curves are to guide the eye. (c) The 'photoemission structure factor' $|M_C(\boldsymbol{k})|^2$ over a wider $\boldsymbol{k}$-space.

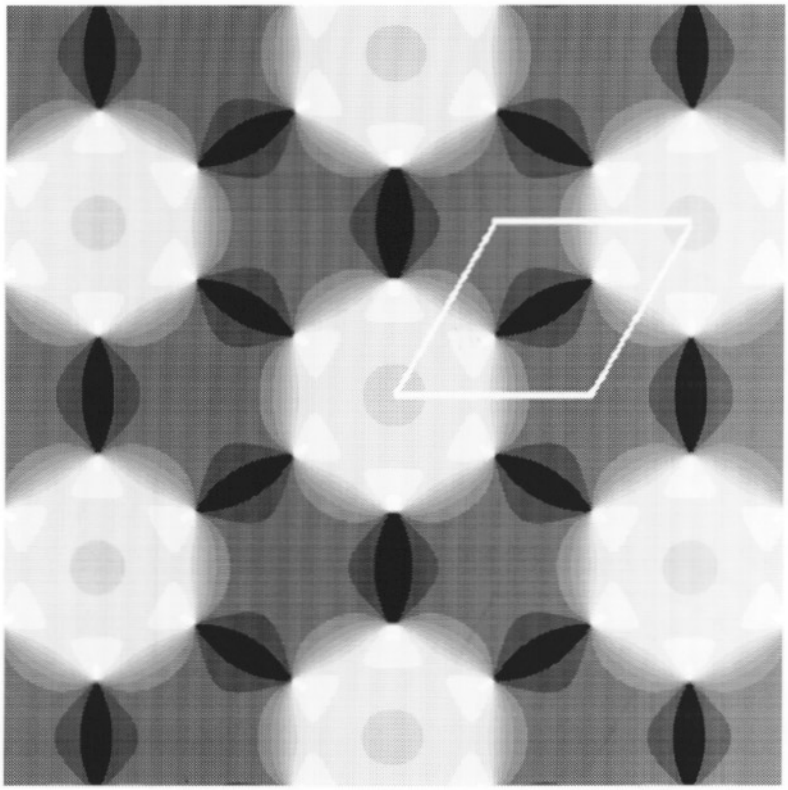

(c)

Figure 8. (Continued)

much deeper than other evaluations. Judging from the distribution in figure 7(d), the pattern in figure 4(o) is truncated in the central vertical zone according to equation (14) and may not accurately reflect the band dispersion. This result suggests that a complementary use of the p-polarized light is sometimes useful for proper evaluation of the band dispersion.

5.2. Wave-vector-dependent interference effects

The photoelectron angular distribution from the π-band, $I^{\pi}(\theta_{\boldsymbol{k}}, \phi_{\boldsymbol{k}})$, is written as

$$I^{\pi}(\theta_{\boldsymbol{k}}, \phi_{\boldsymbol{k}}) \propto |M_C(\boldsymbol{k})|^2 \, |\sin\theta_{\boldsymbol{k}} \cos\theta_{\boldsymbol{k}} \cos\phi_{\boldsymbol{k}}|^2 \tag{15}$$

where $M_C(\boldsymbol{k})$ is represented by (10). The inequivalence between different BZ comes from this $M_C(\boldsymbol{k})$-term including the coefficients of atomic orbitals. A similar result was very recently reported by Shirley *et al* [19].

$I^{\pi}(\theta_{\boldsymbol{k}}, \phi_{\boldsymbol{k}})$ and $|M_C(\boldsymbol{k})|^2$ are plotted in figures 8(a) and 8(b), respectively. When we plot in the (k_x, k_y) plane, the angular dependence of $|M_C(\boldsymbol{k})|^2$ is energy independent because it is a function of only (k_x, k_y). This function is a periodic function with a period of $\sqrt{3} \times \sqrt{3}$ R30° of the network of the BZ as shown in figure 8(c), which means that it repeats in every second-nearest-neighbour BZ. This behaviour originates from the interference induced by the phase difference in the coefficients of the atomic orbitals at the two inequivalent atoms in the unit cell in the initial state. The difference in periodicity

between the bulk BZ and this function is the origin of the inequivalence of the intensity distribution between the first and the second BZ. When the unit cell of the real space is composed of more than two atoms, this kind of interference always occurs. In other words, the distribution in figures 8(b) and 8(c) is an intensity distribution of photoelectrons in a reciprocal space. This concept of an $M_C(\boldsymbol{k})$-distribution is similar to the structure factor distribution in the reciprocal space in the x-ray or electron diffraction studies. Hence, we can call it as a 'structure factor in photoemission' [20].

Comparing figures 7(a) and 8(a), it can be recognized that the gross features of the intensity distribution—for example, the disappearance of the intensity in the central vertical region—are determined mainly by the angular distribution from the atomic orbital as shown in figure 7(a), but considerably modified by the 'structure factor in photoemission' in figure 8(a). The main difference between figure 7(a) and 8(a) is the presence of the dark area in the second BZ—in particular, just outside the bright regions near the K points on the left- and right-hand sides. Here one should notice that $g/|g|$ suddenly changes from $+1$ to -1 because g crosses zero at the K point. Physically speaking, the wave from the A_1-site atoms and that from the A_2-site atoms interfere positively in the first BZ, but they interfere negatively beyond the K point.

Figures 9(b)–9(f) show the simulated photoelectron angular distribution patterns obtained by considering the dispersion given by equation (4) and the intensity given by equation (15). Figures 9(b)–9(f) correspond to figures 4(b)–4(f), having binding energies from 0.7 eV to 4.7 eV in 1.0 eV steps. Figures 9(b) and 9(c) show that the intensity of the π-band is stronger within the first BZ, reproducing the data from this experiment well, i.e., the patterns in figures 4(b) and 4(c). Other figures (figures 9(d)–9(f)) also show reasonable explanations of the experimentally observed inequivalent intensity distributions in the first and second BZ.

In figure 4(a) we observed a finite size of the bright region near the K point. The centre of gravity of the bright region is slightly inside the first BZ, in contradiction to the commonly accepted idea that the Fermi surface exists on or very near the K point. According to the prediction that the π-band photoemission is stronger in the first BZ than in the second BZ near the K points, as revealed in figures 9(b) and 9(c), the centre of gravity of the bright regions may be observed slightly inside the first BZ edge. In this way, most unusual experimental results are consistently interpreted by considering the interference effect.

Pescia *et al* [21] reported a new selection rule for the two π-bands of graphite in the normal-photoemission configuration. They have found a wavevector dependence of the symmetry of the photoelectron final state and the inequivalence of different BZ on a high-symmetry axis. If we consider the interaction between layers and two π-bands, we can automatically include the equivalent effect in the expression for $M_C(\boldsymbol{k})$. Although the group theoretical treatment [21] is limited to high-symmetry points in the BZ, our present model can handle the whole region of the extended BZ and is more generally applicable to two-dimensional photoelectron angular distribution studies.

6. Conclusion

We have directly observed contours of the two-dimensional bands and the Fermi surface of single-crystal graphite. The patterns at various binding energies have shown crystal-symmetry-broken photoelectron distribution patterns and uneven intensities in different Brillouin zones. These prominent features are well explained by a model including the tight-binding initial state and a free-electron-like final state. The non-sixfold symmetry is primarily understood as the result of the angular dependence of the dipole transition

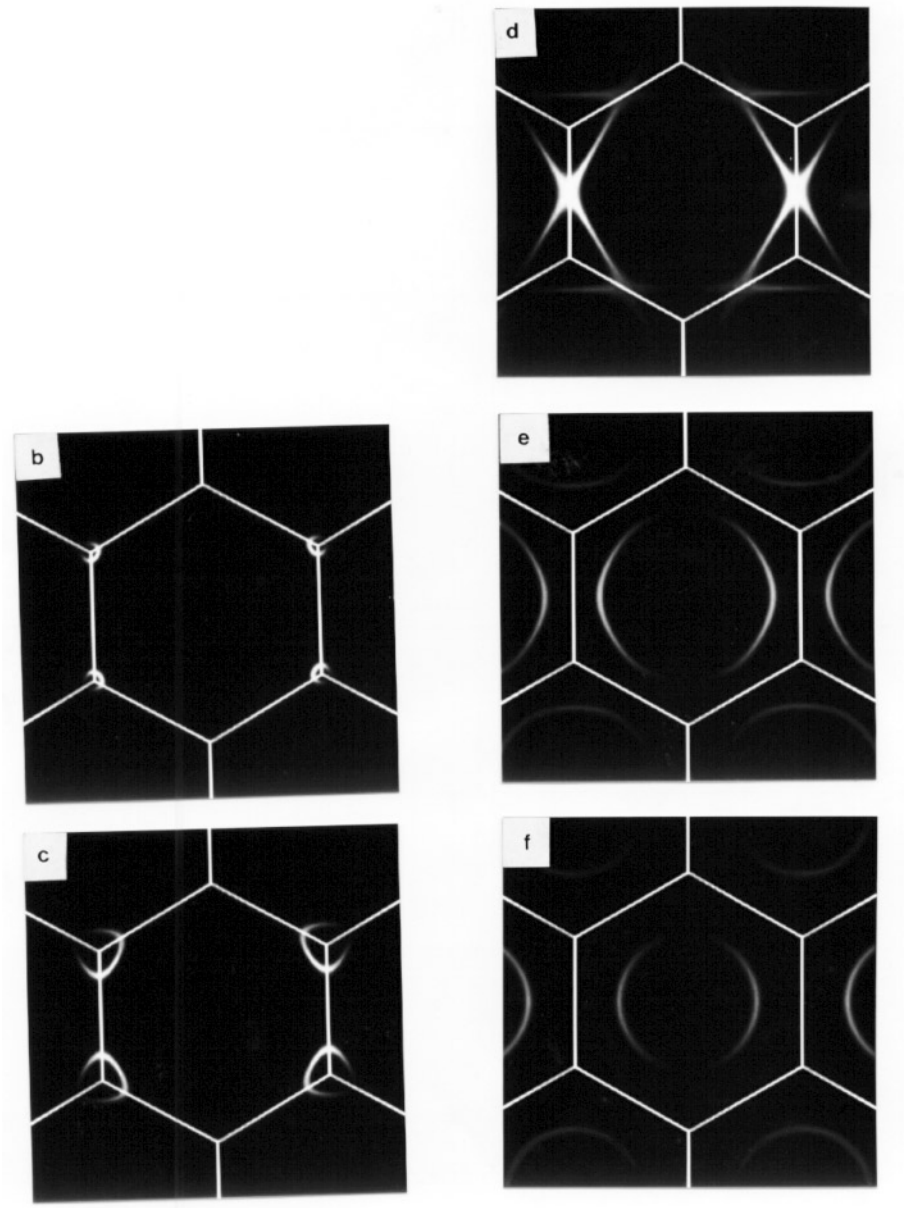

Figure 9. Simulated photoelectron angular distribution patterns of the π-band for E_B larger than 0.7 eV: (b) $E_B = 0.7$, (c) 1.7, (d) 2.7, (e) 3.7 and (f) 4.7 eV, which correspond to the experimental spectra shown in figures 4(b), 4(c), 4(d), 4(e) and 4(f), respectively (the simulation for figure 4(a) is not shown).

probability for transitions from the initial-state atomic orbital with a particular symmetry (p_z, p_y, p_x and s) for the s-polarized radiation. Hence, the two-dimensional measurement can not only provide the band contour at any value of E_B but also allows us to deduce the symmetry of the initial state. The uneven intensity in different BZ is found to be induced by

the interference originating from the phase difference in the two coefficients of the atomic orbitals at inequivalent atoms in the unit cell in the initial state. This idea is described as a 'structure factor in photoemission'.

Acknowledgments

The authors would like to thank Professor Suematsu and Dr Murakami, of the University of Tokyo, for providing us with the kish graphite sample. The helpful discussions with Professor K Cho of Osaka University and Professor R Saito of the University of Electro-Communications are gratefully acknowledged. The authors are much obliged to Professor T Miyahara and Dr Y Kagoshima of the Photon Factory, KEK and Professor T Ohta and Dr H Namba of the Department of Chemistry of the University of Tokyo for their advice and support. This work was performed under the approval of the Photon Factory Programme Advisory Committee and supported by a Grant-in-Aid for Scientific Research from the Ministry of Education, Science, Sports and Culture, Japan.

References

[1] Himpsel F J, Terminello L J, Lapiano-Smith D A, Eklund E A and Barton J J 1992 *Phys. Rev. Lett.* **68** 3611
[2] Aebi P, Osterwalder J, Fasel R, Naumovic D and Schlapbach L 1994 *Surf. Sci.* **307** 917
[3] Chambers S A 1992 *Surf. Sci. Rep.* **16** 261
[4] Daimon H 1988 *Rev. Sci. Instrum.* **59** 545; 1990 *Rev. Sci. Instrum.* **61** 205
Daimon H and Ino S 1990 *Rev. Sci. Instrum.* **61** 57
Nishimoto H, Daimon H, Suga S, Tezuka Y, Ino S, Kato I, Zenitani F and Soezima H 1993 *Rev. Sci. Instrum.* **64** 2857
[5] Eastman D E, Donelon J J, Hien N N and Himpsel F J 1980 *Nucl. Instrum. Methods* **172** 327
[6] Law A R, Johnson M T and Hughes H P 1986 *Phys. Rev.* B **34** 4289
[7] Takahashi T, Tokailin H and Sagawa T 1985 *Phys. Rev.* B **32** 8317
[8] Papagno L and Caputi L S 1983 *Surf. Sci.* **125** 530
[9] Santoni A, Terminello L J, Himpsel F J and Takahashi T 1991 *Appl. Phys.* A **52** 299
[10] Bernal J D 1924 *Proc. R. Soc.* A **106** 749
[11] Saito R, Fujita M, Dresselhaus G and Dresselhaus M S 1992 *Phys. Rev.* B **46** 1804
[12] Bouckaert L P, Smoluchowski R and Wigner E 1936 *Phys. Rev.* **50** 58
[13] Tatar R C and Rabii S 1982 *Phys. Rev.* B **25** 4126
[14] Williams P M 1977 *Nuovo Cimento* B **38** 216
[15] Eberhardt W, McGovern I T, Plummer E W and Fisher J E 1980 *Phys. Rev. Lett.* **21** 200
[16] Goldberg S M, Fadley C S and Kono S 1981 *J. Electron Spectrosc. Relat. Phenom.* **21** 285
[17] Gadzuk J W 1975 *Phys. Rev.* B **12** 5608
[18] Nishimoto H, Okuda T, Nakatani T, Daimon H, Matsushita T, Imada S, Suga S, Namba H, Ohta T, Kagoshima Y and Miyahara T 1996 *Solid State Commun.* at press
[19] Shirley E L, Terminello L J, Santoni A and Himpsel F J 1995 *Phys. Rev.* B **51** 13 614
[20] Daimon H, Nishimoto H, Imada S and Suga S 1996 *Proc. ICES-6 (Rome)* to be published
[21] Pescia D, Law A R, Johnson M T and Hughes H P 1985 *Solid State Commun.* **56** 809